

A separated vortex ring underlies the flight of the dandelion

Cathal Cummins^{1,2,3}, Madeleine Seale^{2,3,4}, Alice Macente^{2,4,5}, Daniele Certini¹, Enrico Mastropaoletti⁴, Ignazio Maria Viola^{1*} & Naomi Nakayama^{2,3,6*}

Wind-dispersed plants have evolved ingenious ways to lift their seeds^{1,2}. The common dandelion uses a bundle of drag-enhancing bristles (the pappus) that helps to keep their seeds aloft. This passive flight mechanism is highly effective, enabling seed dispersal over formidable distances^{3,4}; however, the physics underpinning pappus-mediated flight remains unresolved. Here we visualized the flow around dandelion seeds, uncovering an extraordinary type of vortex. This vortex is a ring of recirculating fluid, which is detached owing to the flow passing through the pappus. We hypothesized that the circular disk-like geometry and the porosity of the pappus are the key design features that enable the formation of the separated vortex ring. The porosity gradient was surveyed using microfabricated disks, and a disk with a similar porosity was found to be able to recapitulate the flow behaviour of the pappus. The porosity of the dandelion pappus appears to be tuned precisely to stabilize the vortex, while maximizing aerodynamic loading and minimizing material requirements. The discovery of the separated vortex ring provides evidence of the existence of a new class of fluid behaviour around fluid-immersed bodies that may underlie locomotion, weight reduction and particle retention in biological and manmade structures.

Dandelions (*Taraxacum officinale* agg.) are highly successful perennial herbs that can be found in temperate zones all over the world⁵. Dandelions, as with many other members of the Asteraceae family, disperse their bristly seeds using the wind and convective updrafts^{6,7}. Most dandelion seeds probably land within 2 m^{8,9}; however, in warmer, drier and windier conditions, some may fly further (up to 20,000 seeds per hectare travelling more than 1 km by one estimate)^{6,10}. Asteraceae seeds routinely disperse over 30 km and occasionally even 150 km^{3,4}.

Plumed seeds comprise a major class of dispersal strategies used by numerous and diverse groups of flowering plants, of which the common dandelion is a representative example. Plumed seeds contain a bundle of bristly filaments, called a pappus, which are presumed to function in drag enhancement (Fig. 1a–c). The pappus prolongs the descent of the seed, so that it may be carried further by horizontal winds¹¹, and may also serve to orientate the seed as it falls^{7,12}.

Dandelion seeds fall stably at a constant speed in quiescent conditions^{2,13–15}. For wind-dispersed seeds, maintaining stability while maximizing descent time in turbulent winds may be useful for long-distance dispersal^{16,17}. It is not clear, however, why plumed seeds have opted for a bristly pappus rather than a wing-like membrane, which is known to enhance lift in some other species (for example, maples¹). Here we analyse the flight mechanism of the dandelion by characterizing the fluid dynamics of the pappus and identifying the key structural features enabling its stable flight.

To examine the flow behaviour around the pappus, we built a vertical wind tunnel (Fig. 1d and Methods), which was designed so that the seed can hover at a fixed height. The flow past the pappus was visualized for both freely flying (Supplementary Video 1) and fixed

(Fig. 1e, f and Supplementary Videos 2, 3) samples, using long-exposure photography and high-speed imaging. We found a stable air bubble (a vortex ring) that is detached from the body, yet steadily remains a fixed distance downstream of the pappus (Fig. 1e, f and Extended Data Figs. 1a–j, 2a–j, 3a–d). Bluff bodies (such as circular disks) may generate vortex rings in their wake, but these are either attached to the body or shed from it and advected downstream. The vortex ring in the wake of the pappus is neither attached nor advected downstream, and we therefore called this vortex a separated vortex ring (SVR). The topology of SVRs has been considered theoretically, but was thought to be too unstable to actually occur¹⁸; here we show that the design of the pappus stabilizes the SVR.

Attached vortex rings form behind circular obstacles; however, it is unclear how the pappus can generate a vortex ring with such a limited air–structure interface (that is, high porosity). The morphology of the dandelion seeds was determined using X-ray computed microtomography (μ CT) and light microscopy (Fig. 1a–c and Methods). The pappus was found to comprise $n = 100$ filaments (95–106 (mean (95% confidence interval)); $n = 10$ seeds) that radiate out from a central point (the pulvinus), each with a mean length (L) of 7.4 mm (7.35–7.46 mm (95% confidence interval); $n = 937$ filaments; Fig. 1a, b) and mean diameter (d) of 16.3 μ m (15.7–17.0 μ m (95% confidence interval); $n = 10$ filaments; Fig. 1c). The porosity (ε , defined as the ratio of the empty projected area to the plan area of the enclosing disk) of the pappus was measured using light microscopy (Methods) and was found to be 0.916 (0.907–0.923 (mean (95% confidence interval); $n = 10$ seeds).

The Reynolds number is a non-dimensional parameter characterizing the relative importance of inertial to viscous forces in a fluid. The flow through and around the pappus involves two different Reynolds numbers: that of the entire pappus ($Re = UD/\nu$, in which U is the velocity of the seed, D is the diameter of the pappus and ν the kinematic viscosity of the fluid) and that of an individual filament ($Re_f = Ud/\nu$). Our modelling revealed that the pappus of a dandelion benefits from a ‘wall effect’^{19,20} at low Re_f (Methods). Neighbouring filaments interact strongly with one another because of the thick boundary layer around each filament, which causes a considerable reduction in air flow through the pappus (Methods). This effect—which was previously considered to be unimportant for dandelion seeds^{2,21}—confers the high drag coefficient of the seed, which helps the seed to remain aloft.

The drag coefficient ($C_D = F/0.5\rho U^2 A$, in which F is the drag force acting on the seed, ρ is the density of air and A is the projected area of the pappus) of the dandelion seeds was calculated by measuring the terminal velocity $U = 39.1 \text{ cm s}^{-1}$ (34.9–43 cm s^{-1} ; mean (95% confidence interval); $n = 10$ seeds) in a drop test (Fig. 2a). The seeds were ballasted and cut to vary the weight to explore a wide range of Re (Methods). The mean diameter of the dandelion pappi in our drop tests was $D = 13.8 \text{ mm}$ (13.2–14.3 mm (95% confidence interval); $n = 10$ seeds). With a mean porosity of $\varepsilon = 0.916$, the total projected area of

¹School of Engineering, Institute for Energy Systems, University of Edinburgh, Edinburgh, UK. ²School of Biological Sciences, Institute of Molecular Plant Sciences, University of Edinburgh, Edinburgh, UK. ³SynthSys Centre for Systems and Synthetic Biology, University of Edinburgh, Edinburgh, UK. ⁴School of Engineering, Institute for Integrated Micro and Nano Systems, University of Edinburgh, Edinburgh, UK. ⁵School of Geographical and Earth Sciences, University of Glasgow, Glasgow, UK. ⁶Centre for Science at Extreme Conditions, University of Edinburgh, Edinburgh, UK.
*e-mail: i.m.viola@ed.ac.uk; naomi.nakayama@ed.ac.uk

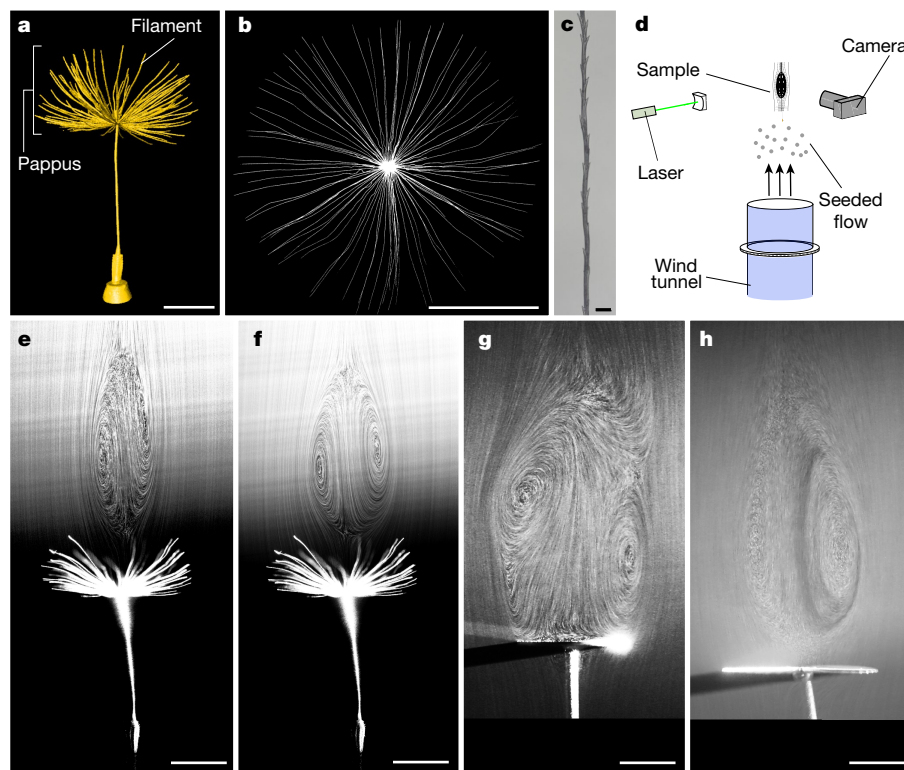


Fig. 1 | The dandelion seed and the vortex that it generates.

a–c, Structural features of the drag-generating pappus at multiple scales: the μ CT scan of a dandelion seed (**a**), the top-down view of the pappus (**b**) and the light microscopy image of a section of a filament (**c**). **d, e,** A vertical wind tunnel (**d**) was used to visualize the steady vortex downstream of a dandelion seed (**e**) at the terminal velocity of a seed.

the pappus is $A = 12.6 \text{ mm}^2$ ($11.5\text{--}13.5 \text{ mm}^2$). For a solid disk to supply the same drag force (that is, with a mean weight (W) of $6.2 \mu\text{N}$ ($5.51\text{--}6.86 \mu\text{N}$ (95% confidence interval); $n = 10$ seeds) of the seed) as the pappus at the same terminal velocity (see Methods), its diameter is given by $D_{\text{disk}} = \sqrt{8W/(1.17\rho\pi U^2)} = 8.6 \text{ mm}$, which is 38% smaller than D . The Re of the pappus is 357, whereas the equivalent disk has an Re of 222.

The ratios of the equivalent disk diameter (D_{disk}) and area (A_{disk}) to the pappus diameter (D) and area (A), respectively, indicate that the equivalent disk is always smaller, but has a significantly higher projected area than the pappus (Fig. 2b). Thus, the pappus delivers more than four times the amount of drag per unit area compared to a solid disk²², which quadruples C_D . The pappus achieves this effect through the interaction between the thick boundary layers surrounding each filament (Methods). In terms of material requirement, the pappus has a volume of less than 77.5 pm^3 (given that individual filaments are more than 50% hollow¹⁵). An equivalent impervious membrane of this volume would be about $1 \mu\text{m}$ in thickness, which is far thinner than the wings of flying seeds¹⁴, although the composition of the material may also affect the efficiency of construction.

The existence of the SVR and the elevated drag coefficient are a consequence of the filaments considerably reducing the flow through the pappus, decreasing its permeability. In turn, the pressure downstream of the pappus is reduced, which increases the drag on the pappus (Methods). We measured the flow using particle image velocimetry (PIV, Methods) in the vortex downstream of the dandelion pappus (Fig. 3a–c); the magnitude of the maximum reverse flow was about 10% of the freestream velocity. We distinguished between attached and separated stable vortex rings based on the position of the upstream stagnation point (z_{su}): if $z_{\text{su}} > 0$, the vortex is separated (see Fig. 3a); otherwise it is attached.

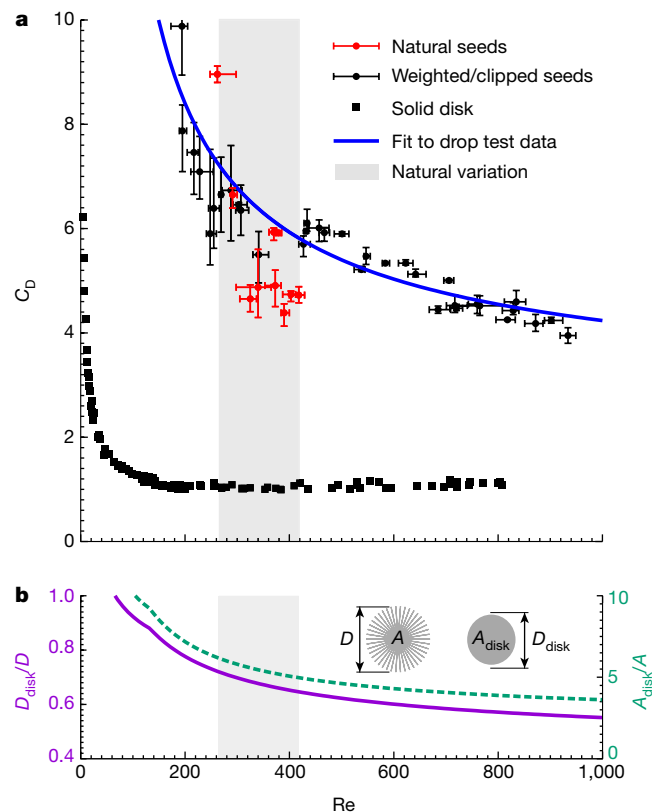
f, g, h, At 60% of the terminal velocity, the vortex is slightly larger and more symmetric, showing the structure of the separated vortex ring more clearly. **g, h,** In the same flow conditions as **e** and **f**, solid and porous disks generate vortex shedding (**g**) and a separated vortex ring (**h**), respectively. Scale bars, $50 \mu\text{m}$ (**c**) or 5 mm (all other panels).

To explore the effects of porosity, silicon disks mimicking the pappus were microfabricated, for which the degree of the porosity varied from 0 (that is, impervious) to 0.92 (comparable to a pappus) (Methods and Extended Data Fig. 4a–p). The disks were held fixed in position in the vertical wind tunnel, and flow visualization was used to explore the flow dynamics across the same range of Re as for our biological samples (for example, Fig. 1g, h). All disks generated a prominent recirculating wake (Fig. 3d–f and Supplementary Videos 4, 5). As ε increases, this vortex detaches from the disk to form an SVR. The structure and nature of the vortex depends on Re and ε . For low Re, the vortex is axisymmetric, but it loses this symmetry as Re increases. This was also observed on the dandelion pappus (Fig. 1e, f).

Our PIV analysis revealed that the magnitude of the maximum reverse flow for disks is on the order of 10% of the freestream velocity, which is in good agreement with our analysis of the flow around the biological samples (Fig. 3a–c). In both the disks and the biological samples, the streamwise length of the SVR is equal to about one characteristic diameter (disk and pappus diameter, respectively).

The SVR is not always steady; for a given porosity ε , there is a critical Reynolds number (Re_c) at which the SVR breaks down into periodic vortex shedding (Extended Data Fig. 5a–l and Supplementary Discussion). We measured Re_c for the dandelion seeds and porous disks (Methods). For the impervious disk, the measured Re_c (149 ± 2 , combined the mean \pm s.e.m. of velocity, diameter and kinematic viscosity measurements) is consistent with existing results of direct numerical simulations^{23,24}, therefore validating our experimental methodology.

Identification of Re_c for the disks and dandelion samples (Fig. 4a) revealed that Re_c generally increases with increasing ε . Figure 4a, b shows the boundary in the Re – ε parameter space that separates regions of steady SVRs and unsteady vortex shedding for porous disks. The mean measured Re_c for dandelion seeds was $Re_c = 429$ ($415\text{--}440$ (95% confidence interval); $n = 10$), which is in good agreement with the Re_c



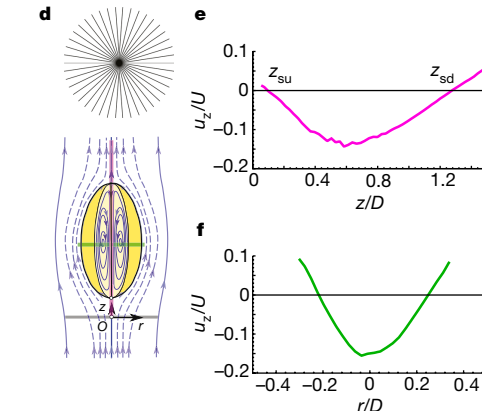
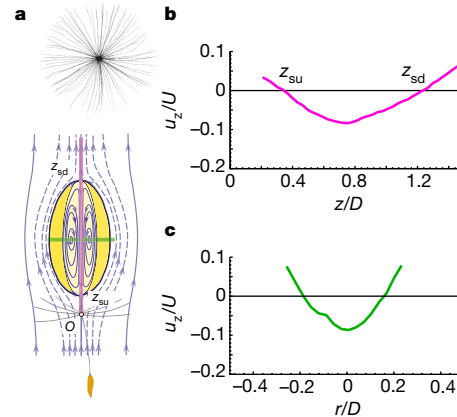
value of 457 ± 5 (combined mean \pm s.e.m. of velocity, diameter and kinematic viscosity measurements) that was found for a porous disk with identical porosity (see Methods). This result indicates that, despite its geometric complexity spreading in height, the pappus acts as if it is a flat circular disk with the same porosity.

All of the dandelion samples that we tested flew at a Re below Re_c (Fig. 4b). This suggests that evolution has tuned the pappus porosity to eliminate vortex shedding as the seed flies. Therefore, the filamentous design of plumed seeds confers two major advantages compared to a membranous one: a fourfold increase in the loading and an enhancement of the flight stability. This makes the plumed design far more efficient at flying than a membrane (that is, a circular disk) for lightweight seeds.

Traditional mathematical models of the pappus of a dandelion seed rely on the assumption that each of the filaments of the seed can be treated as a translating cylinder, with the total drag on the pappus being the sum of the contributions from each filament^{2,14}. However, our numerical modelling and experimental measurements revealed that the flow through the seed entails strong interactions between neighbouring filaments^{19,20}, causing the pappus to behave as a permeable membrane. It has been suggested that changing the permeability of a body could be useful to control or suppress the vortex shedding²⁵. A recent study has confirmed that the motion of freely falling disks (with $Re > 10^3$) can be stabilized by a hole in the centre of the disk²⁶. An oscillating wake is a necessary contributing factor for the unsteady motion of falling disks²⁶, and the dandelion seed has eliminated this oscillation by evolving a pappus with a high porosity, thus enabling steady flight.

The initial motion of dandelion seeds is brief but fast, and is rapidly stabilized¹⁵ into an equilibrium orientation that minimizes the terminal velocity of the seed, allowing the seed to make maximal use of updrafts¹⁷. Our experiments demonstrate that the stabilization of plumed seeds is not guaranteed by an arbitrarily porous pappus, as was previously suggested^{11,12}. Instead, stability is gained by tuning the porosity of the pappus.

There are two major types of wind-dispersed seeds, which are distinguished by their appendage (winged or plumed) or equally by their flight mechanism (lift- or drag-based, respectively)¹⁴. The preferred mode of flight for large seeds—such as the maple seed—is winged^{1,2}, where high lift forces are attained by a leading-edge vortex. The leading-edge vortex reduces the pressure on the upper face of the wing, enhancing lift compared with non-rotating winged seeds. For winged seeds, greater release heights are necessary to reach the stable lift-generating phase. Therefore, winged flight is probably not effective for the dispersal of small and light seeds of short plants. Instead, the bristly pappus



and the radial coordinate r . **b, c**, The axial velocity u_z was measured along the z (magenta) and r (green) directions with PIV (**b** and **c**, respectively). Note that u_z is non-dimensionalized with U , whereas z and r are non-dimensionalized with D . **d–f**, The same as **a–c** for a disk with a porosity of 0.89 and a computer-aided design drawing of the porous disk in plan view (**d**, top). **e, f**, Data were obtained for a single disk.

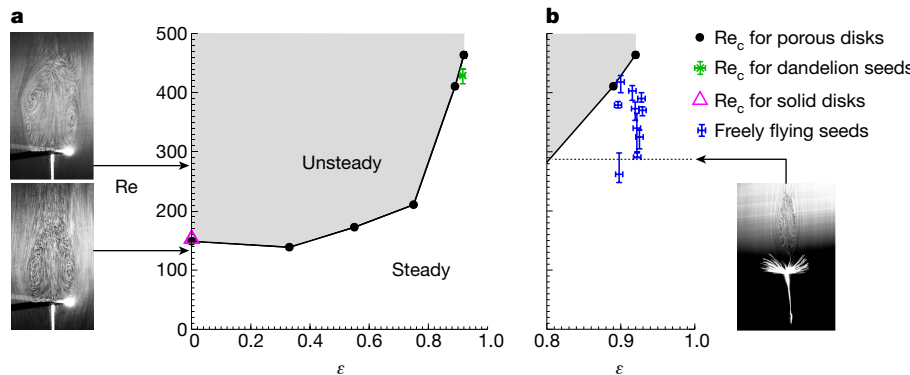


Fig. 4 | The loss of stability of the wakes past porous disks and dandelion seeds. **a**, The limiting Reynolds number at which the wake becomes unstable (Re_c) is plotted on the Re - ε plane for porous silicon disks. The mean Re_c for the dandelion samples (green), and values from the literature²³ for solid disks (magenta). The green data point shows the mean and 95% confidence intervals, $n = 10$ independent biological repeats. Each black dot is obtained from data from a single disk at the

stated porosity. **b**, A zoomed-in region for $0.8 < \varepsilon < 1$, on which the measured values of Re and ε for freely flying dandelion seeds (blue) are superimposed. Blue data are mean and 95% confidence intervals, $n = 10$ independent biological repeats. Data for Reynolds numbers are identical to those in Fig. 2a. Insets show snapshots of the flow at the indicated Re behind solid disks (left side) and dandelion pappus (right side).

of the dandelion enhances its flight capacity through drag using a completely different type of vortex.

The shift from membranous to bristle-based flight occurs in animals, too: very small insects (for example, *Thrips physapus* L.) have evolved bristly wings rather than membranous ones^{20,27–29}. Flight at this scale makes use of a technique called ‘clap and fling’, and bristly wings reduce the force required to fling the wings apart^{28,30}. These insects can also float by spreading out their wings, generating 90% of the wing loading of a solid plate with 10% of the material²⁰. Bristly appendages are common among light-weight fliers and swimmers, and it is likely that the SVR and similar permeability-dependent vortices have a crucial role in their locomotion. They may also underlie the feeding mechanisms of underwater organisms, such as the larvae of the black fly (*Simulium vittatum*), which use a bristly fan for suspension feeding^{31,32}. Because Re_c shifts with the degree of porosity, small changes in the morphology of their appendages may markedly affect the dynamics of this vortex, leading to a switch in their biological function, for example, from foraging to escape³³.

By uncovering the physics behind the flight of the dandelion, we have discovered a novel type of fluid behaviour around fluid-immersed bodies. As filamentous microstructures within the relevant Re regimes (<1 for the pore scale and about 100–1,000 for the body scale) are commonplace in the biological world^{19,31,34}, we anticipate that permeability-dependent flow control is prevalent in nature. Traditionally, fluid dynamics investigations tend to observe a single Re scale; exploration of interactions among multiple Re regimes may uncover other as yet unknown fluid behaviours.

Online content

Any methods, additional references, Nature Research reporting summaries, source data, statements of data availability and associated accession codes are available at <https://doi.org/10.1038/s41586-018-0604-2>.

Received: 19 April 2018; Accepted: 21 August 2018;

Published online 17 October 2018.

- Lentink, D., Dickson, W. B., van Leeuwen, J. L. & Dickinson, M. H. Leading-edge vortices elevate lift of autorotating plant seeds. *Science* **324**, 1438–1440 (2009).
- Greene, D. F. & Johnson, E. A. The aerodynamics of plumed seeds. *Funct. Ecol.* **4**, 117–125 (1990).
- Ridley, H. N. On the dispersal of seeds by wind. *Ann. Bot.* **os-19**, 351–364 (1905).
- Small, J. The origin and development of the Compositae. *New Phytol.* **17**, 200–230 (1918).
- Holm, L. G. *World Weeds: Natural Histories and Distribution* (John Wiley & Sons, New York, 1997).
- Tackenberg, O., Poschlod, P. & Kahmen, S. Dandelion seed dispersal: the horizontal wind speed does not matter for long-distance dispersal—it is updraft! *Plant Biol.* **5**, 451–454 (2003).
- Sheldon, J. & Burrows, F. The dispersal effectiveness of the achene–pappus units of selected Compositae in steady winds with convection. *New Phytol.* **72**, 665–675 (1973).
- Nathan, R. et al. Mechanisms of long-distance seed dispersal. *Trends Ecol. Evol.* **23**, 638–647 (2008).
- Soons, M. B. & Ozinga, W. A. How important is long-distance seed dispersal for the regional survival of plant species? *Divers. Distrib.* **11**, 165–172 (2005).
- Greene, D. F. The role of abscission in long-distance seed dispersal by the wind. *Ecology* **86**, 3105–3110 (2005).
- Andersen, M. C. An analysis of variability in seed settling velocities of several wind-dispersed Asteraceae. *Am. J. Bot.* **79**, 1087–1091 (1992).
- Burrows, F. Calculation of the primary trajectories of plumed seeds in steady winds with variable convection. *New Phytol.* **72**, 647–664 (1973).
- Andersen, M. C. Diaspore morphology and seed dispersal in several wind-dispersed Asteraceae. *Am. J. Bot.* **80**, 487–492 (1993).
- Minami, S. & Azuma, A. Various flying modes of wind-dispersed seeds. *J. Theor. Biol.* **225**, 1–14 (2003).
- Sudo, S., Matsui, N., Tsuyuki, K. & Yano, T. Morphological design of dandelion. In *Proc. 11th International Congress and Exposition* (Society for Experimental Mechanics, 2008).
- Tackenberg, O., Poschlod, P. & Bonn, S. Assessment of wind dispersal potential in plant species. *Ecol. Monogr.* **73**, 191–205 (2003).
- Stevenson, R. A., Evangelista, D. & Looy, C. V. When conifers took flight: a biomechanical evaluation of an imperfect evolutionary takeoff. *Paleobiology* **41**, 205–225 (2015).
- Délier, J. *Three-Dimensional Separated Flows Topology: Singular Points, Beam Splitters and Vortex Structures* (John Wiley & Sons, 2013).
- Vogel, S. *Life in Moving Fluids: The Physical Biology of Flow* (Princeton Univ. Press, Princeton, 1981).
- Barta, E. & Weihs, D. Creeping flow around a finite row of slender bodies in close proximity. *J. Fluid Mech.* **551**, 1–17 (2006).
- Casseau, V., De Croon, G., Izzo, D. & Pandolfi, C. Morphologic and aerodynamic considerations regarding the plumed seeds of *Tragopogon pratensis* and their implications for seed dispersal. *PLoS ONE* **10**, e0125040 (2015).
- Roos, F. W. & Willmarth, W. W. Some experimental results on sphere and disk drag. *AIAA J.* **9**, 285–291 (1971).
- Shenoy, A. & Kleinstreuer, C. Flow over a thin circular disk at low to moderate Reynolds numbers. *J. Fluid Mech.* **605**, 253–262 (2008).
- Fernandes, P. C., Rizzo, F., Ern, P. & Magnaudet, J. Oscillatory motion and wake instability of freely rising axisymmetric bodies. *J. Fluid Mech.* **573**, 479–502 (2007).
- Cummins, C., Viola, I. M., Mastropaoletti, E. & Nakayama, N. The effect of permeability on the flow past permeable disks at low Reynolds numbers. *Phys. Fluids* **29**, 097103 (2017).
- Vincent, L., Shambaugh, W. S. & Kanso, E. Holes stabilize freely falling coins. *J. Fluid Mech.* **801**, 250–259 (2016).
- Davidi, G. & Weihs, D. Flow around a comb wing in low-Reynolds-number flow. *AIAA J.* **50**, 249–253 (2012).
- Jones, S. K., Yun, Y. J. J., Hedrick, T. L., Griffith, B. E. & Miller, L. A. Bristles reduce the force required to ‘fling’ wings apart in the smallest insects. *J. Exp. Biol.* **219**, 3759–3772 (2016).
- Lee, S. H. & Kim, D. Aerodynamics of a translating comb-like plate inspired by a fairyfly wing. *Phys. Fluids* **29**, 081902 (2017).
- Santhanakrishnan, A. et al. Clap and fling mechanism with interacting porous wings in tiny insect flight. *J. Exp. Biol.* **217**, 3898–3909 (2014).
- Cheer, A. & Koehl, M. Paddles and rakes: fluid flow through bristled appendages of small organisms. *J. Theor. Biol.* **129**, 17–39 (1987).
- Ross, D. H. & Craig, D. A. Mechanisms of fine particle capture by larval black flies (Diptera: Simuliidae). *Can. J. Zool.* **58**, 1186–1192 (1980).

33. van Duren, L. A. & Videler, J. J. Escape from viscosity: the kinematics and hydrodynamics of copepod foraging and escape swimming. *J. Exp. Biol.* **206**, 269–279 (2003).
34. Seale, M., Cummins, C., Viola, I. M., Mastropaoletti, E. & Nakayama, N. Design principles of hair-like structures as biological machines. *J. R. Soc. Interface* **15**, 20180206 (2018).

Acknowledgements This work was supported by the Leverhulme Trust (RPG-2015-255) and the Royal Society (UF140640). We thank I. Butler (Geosciences, University of Edinburgh) for assistance with the μ CT scans; and A. Firth and M. Mason (Engineering, University of Edinburgh) for helping to build the wind tunnel.

Reviewer information *Nature* thanks M. Dickinson and the other anonymous reviewer(s) for their contribution to the peer review of this work.

Author contributions C.C., E.M., I.M.V. and N.N. designed the experiments. C.C. designed and set up the wind tunnel. C.C. carried out the numerical analyses, the flight assay and flow visualization with assistance from M.S.

and D.C. C.C. designed and E.M. fabricated the silicon disks. A.M. optimized and performed the μ CT scans, and M.S. analysed the resulting 3D images. C.C. wrote the manuscript; M.S., E.M., I.M.V. and N.N. helped with revision and editing. E.M., I.M.V. and N.N. designed and oversaw the project; I.M.V. supervised the investigations of fluid mechanics and N.N. supervised the biological and structural studies.

Competing interests The authors declare no competing interests.

Additional information

Extended data is available for this paper at <https://doi.org/10.1038/s41586-018-0604-2>.

Supplementary information is available for this paper at <https://doi.org/10.1038/s41586-018-0604-2>.

Reprints and permissions information is available at <http://www.nature.com/reprints>.

Correspondence and requests for materials should be addressed to I.M.V. or N.N.

Publisher's note: Springer Nature remains neutral with regard to jurisdictional claims in published maps and institutional affiliations.

METHODS

Data reporting. No statistical methods were used to predetermine sample size. The experiments were not randomized and the investigators were not blinded to allocation during experiments and outcome assessment.

Experiments using vertical wind tunnel. *Flow visualization.* A vertical wind tunnel was built to visualize the flow around natural and artificial (microfabricated) pappi. Airflow was generated in the wind tunnel using a fan (San Ace 9GA0412P6G001) mounted on the inlet of the tunnel. The fan speed was controlled by pulse wave modulation using an Arduino Uno. The flow conditioning consisted of three meshes of open area ratios: 70%, 66% and 66% and a honeycomb flow straightener. A fog machine (Rosco 1700) was used to seed the air in the wind tunnel, and the flow was illuminated using a 2.5-W diode-pumped continuous wave laser (Medialas DPGL 2500) with a wavelength of 532 nm (Extended Data Fig. 6b).

The videos were obtained using a Canon EOS 70D (for low-speed videos) and a Fastcam Photron SA1 (for high-speed videos)—both with a Tamron 180 mm F3.5 SP AF Di Macro Lens. The flow speed and turbulent intensity ($T_u = u'/U$, in which u' is the root-mean-square of the turbulent velocity fluctuations and U is the mean velocity) was measured using two-dimensional laser Doppler anemometry, comprising a 5-W argon ion laser with a wavelength of 488 nm and Dantec Dynamics FibreFlow optics (Extended Data Fig. 6a). The mean velocity varied from a minimum of 0.19 m s⁻¹ to a maximum of 0.72 m s⁻¹, with a maximum T_u of 3.6% and a mean T_u of 2.3%. The flow past $n = 10$ dandelion seeds—randomly selected from ten different capitula (see ‘Growth of dandelion specimens (*T. officinale* agg.)—flying at their terminal velocity was visualized in the wind tunnel; each seed showed a prominent SVR in its wake (Supplementary Video 1).

The same ten seeds that were used for the freely flying experiments were fixed to trestles, and held fixed in the wind tunnel at different flow speeds; long-exposure photographs of the flow past these seeds were obtained using a Canon EOS 70D. Downstream of each seed, an SVR is present, which is stable across the entire biological variation of the seeds (Fig. 1e, f).

PIV was performed using the CW laser to illuminate air that is seeded with smoke, and a high-speed camera; the data were post-processed using the MATLAB toolbox PIVlab 1.41. The frame rate used in the PIV experiments varied from a minimum of 50 f.p.s. (for low flow-speed experiments) to a maximum of 250 f.p.s. (for high flow-speed experiments). We used a multi-pass linear window deformation technique: the first pass used a 64 × 64-pixel interrogation window, the second pass 32 × 32-pixel interrogation window and sub-pixel displacement was estimated using two-dimensional Gaussian regression. Because we were interested in the flow far from the body, masking was not necessary, and therefore, no masking was used. *Detection of vortex shedding.* The detection of vortex shedding from dandelion samples and replica pappi in the wind tunnel experiments was measured using MATLAB to compute the structural similarity index between a reference frame of the wake region and subsequent frames of the video^{35,36}. The power spectral density estimate of this signal was then found using the covariance method, and the peak frequency f was extracted for a range of Re . A non-zero f indicated the presence of vortex shedding. To compute Re_c for our dandelion seeds, we analysed the flow past $n = 10$ seeds, which were fixed in our wind tunnel. We found that the 95% confidence interval for the mean Re_c for the dandelion samples was $Re_c = 429$ (415–440) (mean (95% confidence interval); $n = 10$ seeds).

To compare the mean Re_c for dandelion samples to the value of Re_c predicted by our porous disks, we linearly interpolated between the data points in Fig. 4b. From this, we estimated that the Re_c of porous disks at the same porosity as our dandelion samples is $Re_c = 457 \pm 5$ (combined mean ± s.e.m. of velocity, diameter and kinematic viscosity measurements) (Fig. 4a, b).

Growth of dandelion specimens (*T. officinale* agg.). Dandelion seeds were collected from a single plant growing in Edinburgh (55.922684°N, 3.170703°W) in April 2014. Seeds were germinated in 10-cm round Petri dishes containing distilled water in 16 h light/8 h dark conditions (100 μmol m⁻² s⁻¹, 25 °C during the day, 23 °C during the night) for two weeks. They were then transplanted to 7 × 7 × 8-cm³ pots with soil/perlite mix 60% v/v Levington's F2+S (Everris), 24% v/v standard perlite (Sinclair), 16% v/v washed horticultural sand 0.3 g l⁻¹ Exemptor (Everris) and grown in 16 h light/8 h dark conditions in a room with a controlled environment (100 μmol m⁻² s⁻¹, 21 °C) for four weeks. Plants were transplanted into 4-l pots with peat/sand mix (83% v/v medium peat (Clover), 21% v/v washed horticultural sand, 3 g l⁻¹ garden limestone (Arthur Bowers), 1 g l⁻¹ Osmocote Exact Standard 5–6 months (Everris), 0.4 g l⁻¹ Exemptor (Everris)) and transferred to a glasshouse with ambient light supplemented to ensure a 16-h day (minimum intensity of 250 μmol m⁻² s⁻¹, 06:00–22:00 GMT) and temperature of 21 °C during the day, 18 °C during the night. For μCT scans, seeds used were the offspring of the original collected plants.

For all other experiments, seeds were from the subsequent generation. All of these seeds from the second generation originated from the same parent plant. As *T. officinale* is apomictic, all seeds are assumed to be genetically identical.

Throughout the paper, we use the term dandelion ‘seed’ to refer to the entire diaspore (fruit–pappus unit).

X-ray computed microtomography (μCT). Ten dandelion samples were individually attached to machined sharpened carbon cones using forceps and cyanoacrylate glue (RS Pro). Samples were sputter-coated with gold for 100–200 s (corresponding to a thickness of approximately 150–300 nm). Scan settings were as shown in Extended Data Table 1.

Data were reconstructed using Octopus 7 software³⁷. The voxel (three-dimensional pixel) size of the reconstructed μCT datasets was 25 μm.

Post-processing of the reconstructed data was carried out with Avizo 9.0.1 (FEI, ThermoFisher Scientific) and R³⁸—see Extended Data Fig. 7 for the workflow chart. Scans were filtered by unsharp masking with a three-voxel kernel size. Small holes of up to 26 voxels were filled and a labelled image was created by interactive thresholding.

For analysis of the pappus geometry, the segmented data were skeletonized using an implementation of the TEASAR algorithm³⁹ (scale = 2.5, constant = 4), in which a tree structure is formed from traced peaks of distance maps and looping is not permitted. The starting point for skeletonization was manually selected for each sample to begin at the central point of the pappus (the pulvinus, where all filaments are attached). Nodes with a coordination number of one (that is, connected to no more than one other node) were considered potential filament end points and nodes were visually inspected to remove false positives from further analysis. A coordinate mapping of each filament was obtained by finding the shortest path between the central starting point and each filament end.

The point coordinates along the length of each filament were smoothed using a Gaussian smoothing filter (window size = 16, $\alpha = 2.5$, tails retained). The window size was selected by stepwise increases of the window size until the mean filament arc length changed by less than 1% from its previous value (that is, interpolation between coordinates of the centre line was no longer significantly affected by noise arising from the limited voxel resolution of the scan). The coordinates of each spatial dimension were separately smoothed with the same settings. Points corresponding to a central disk (the pulvinus) onto which the filaments are attached were removed from further analysis (by removing a central sphere with a radius of 0.56–0.64 mm, depending on the sample), such that only filaments themselves were included.

The spacing between filaments in the pappus was estimated by calculating the distance of the centre line of each filament from the centre line of the nearest neighbouring filament. In total, 93.5% of filaments were correctly segmented, skeletonized and included in the analysis. Spacing was found to linearly increase from zero at the pulvinus to 1.32 mm at the edge of the pappus. This maximum distance divided by two represents the mean distance between filaments, and was an input into the numerical model (creeping flow past an array of filaments). As a small number of filaments were not included, the nearest neighbour calculations represent a slight overestimate. Additionally, it is important to note that these spacing distances are the spacing between centerlines. Filament diameters were at the limit of the resolution of the μCT scanner, so they were not calculated from this data.

Microscopy. *Light microscopy of individual filaments.* All filaments except one were removed from each dandelion fruit. The stalk and pulvinus were stuck onto a glass slide with a small piece of modelling clay such that the single remaining filament lay flat on the slide. Images were acquired with a Nikon E600 fluorescent microscope using a 10× objective, 1-ms exposure, 0.6 gamma and 2× gain. Each field of view was imaged 1–8 times at different focal (z) planes to account for slight changes in topography. Image processing was carried out in ImageJ to calculate filament diameters⁴⁰. Sharp composite images were obtained for each field of view by model-based deconvolution, stitched together with linear blending and converted into binary images^{41,42}. Distance maps were computed and the skeletonized centre line of the filament was overlaid. Diameters were calculated from the distance map at each pixel along the centre line of the filament. The mean of the diameter values at all points along the filament was calculated to give an overall filament diameter. The error in diameter values due to binarization was ± 0.80 μm based on a pixel size of 0.40 μm.

Light microscopy of the entire pappus. The porosity of $n = 10$ dandelion seeds was measured using light microscopy. First, the mean diameter of dandelion pappi (D) were measured using a Dino-Lite digital microscope; the mean diameter was found to be $D = 13.8$ mm (13.2–14.3 mm (95% confidence interval); $n = 10$ seeds). The porosity of these pappi was then measured. The images were obtained using a Nikon SMZ1500 stereomicroscope, with 1× magnification, 38.5-ms exposure, 0.6 gamma, 1.0× gain and 1.60 saturation. The pappi were placed on a glass slide covered with 5 μl of 99% ethanol and were then covered with a glass coverslip. Overlapping sections of each pappus were imaged at different positions on the focal plane to account for the entirety of the pappus. These images were stitched together with linear blending⁴² in ImageJ to form the entire pappus image. The pulvinus was inscribed in a circle to find the centre of the pappus. Images, converted to

RGB colour format, were used to calculate the empty area inside the disk, applying a colour threshold. The porosity (p) of the flattened sample was obtained by calculating the ratio of empty area to the total plan area of the pappus. The porosity ε of the original sample was then calculated to be $\varepsilon = 1 - 2L(1-p)/D = 0.916$ (0.907–0.923) (mean (95% confidence interval); $n=10$ seeds)².

Error analysis using different magnifications. A single filament was removed from a dandelion fruit and placed on a glass slide. The porosity of a rectangular field of view, including a section of the filament, was measured at four different magnifications. From this, the error due to the finite resolution of the equipment was estimated to be 0.54%.

Creeping flow past an array of filaments. The Reynolds number ($Re = UD/\nu$) is calculated using the pappus diameter D as the characteristic length scale, and was found to be in the order of 400. Note, however, that when discussing low-Re effects, a filament Reynolds number, based on a diameter of the filament ($Re_f = Ud/\nu = 0.422$) is used. Because $Re_f < 1$, the equations for creeping flow apply, and may be used to investigate the flow past the pappus. Consider the low Reynolds number flow past a body: it is well-known that the velocity boundary layer attached to the body extends many body diameters into the fluid⁴³, influencing the flow far from it. When this flow interacts with distant boundaries, it is known as a ‘wall effect’. The following estimate of when this effect can be ignored was calculated previously¹⁹:

$$\frac{y}{\lambda} > \frac{20}{Re_f}$$

in which λ is the characteristic length scale of the body and y is the distance to the nearest boundary. In the case of the dandelion, we are considering the effect of neighbouring filaments, so $\lambda = 16.3 \mu\text{m}$, $Re_f = 0.422$ and y is the mean distance between the filaments (see ‘X-ray computed microtomography (µCT)'). To neglect the influence of neighbouring filaments, we can estimate that filaments should be spaced greater than 47 filament diameters apart. However, based on our µCT scan data (see ‘X-ray computed microtomography (µCT)'), the mean distance between the filaments is about 41 filament diameters, therefore, the effects of neighbouring filaments cannot be ignored.

To further confirm this hypothesis, we computed the slow flow (velocity vector (\mathbf{u}) and pressure (P)) past a rectangular array of 100 filaments with a diameter and length equal to those of the dandelion seeds. The filaments within the array were separated by a distance equal to the mean distance between the filaments. We used a previously published modelling approach²⁰. The creeping flow equations

$$\nabla P = \mu \nabla^2 \mathbf{u}$$

$$\nabla \cdot \mathbf{u} = 0$$

were solved in the fluid domain (μ is the dynamic viscosity of the fluid), with each filament represented by a distribution of singularities (Stokeslets with intensity α_i and doublets with intensity β_i) along its axis.

The intensities of the singularities are computed using Wolfram Mathematica 11 by solving an appropriate system of linear equations. We used 64 points that were uniformly distributed along the axis of each body. Once the equations have been solved for \mathbf{u} and p , the drag on each member of the pappus can be computed.

The drag exerted on the i th filament can be expressed in terms of the integral of the Stokeslet intensity along the length of the filament as follows:

$$D_i = 8\pi\mu \int_L \alpha_i(s) ds, \quad i = 1, \dots, m$$

In Extended Data Fig. 8d, the drag on each filament divided by the drag of a single, isolated filament⁴⁴ D_i/D_0 is plotted. We found that there is a strong interaction between filaments. On average, a filament within the pappus experiences a reduction of 84% in drag, compared to an isolated filament. This indicates that the pappus is behaving similar to a continuous surface, substantially reducing the airflow through it. The blockage effects resulting from air being pushed around the pappus are not captured by this model. Therefore, this model cannot be used to explore the resulting flow field around the pappus.

Strictly speaking, this model is valid in the limit as Re_f tends to zero. However, since Re_f is finite, some errors are introduced³¹. Here we examine the error introduced by neglecting the small but finite Re_f for the filaments of the dandelion. The slow flow past an array of slender bodies has previously been analysed²⁷ using computational fluid dynamics for a range of small to moderate Re_f , ranging from 0.01 to 100. This parametric study found that for $Re_f \leq 1$ and spacing of 10 filament diameters, the flow speed between adjacent filaments is identical to the speed found in the previously published Stokes flow model²⁰. The drag force computed using the previously published model²⁰ differed from the force computed the parametric study²⁷, but the trend and order of magnitude remained very similar.

Measurements of C_D . The terminal velocity (U) of $n=10$ dandelion seeds selected randomly from different plants was measured by dropping each seed five times. A DSLR camera (Canon EOS 70D) recorded the fall at 50 f.p.s. over 1 m. The position of the seeds was tracked using MATLAB, and the terminal velocity was found using linear regression of the tracked position data.

Additional masses (strand of polyvinylsiloxane impression material) were attached to the seeds, and the terminal velocity of the composite mass was measured as described above. The mass ((m) consisting of seed + strand) was measured using a Mettler AE 240 analytical balance. To explore the terminal velocity for masses that were lower than the natural mass of the seed, a small part of the seed was cut, and the terminal velocity of this was measured as described above.

The drag coefficient (C_D) was computed using

$$C_D = \frac{mg}{0.5\rho AU^2}$$

in which $\rho = 1.204 \text{ kg m}^{-3}$ is the density of air at normal temperature and pressure, $g = 9.81 \text{ m s}^{-2}$ is the acceleration due to gravity and A is the total projected area of the pappus. By adding masses, the variation in C_D across a wide range of Reynolds numbers of $Re = UD/\nu$, in which $\nu = 15.11 \times 10^{-6} \text{ m}^2 \text{ s}^{-1}$ is the viscosity of air and D is the pappus diameter, was explored.

The mean mass of the dandelion seeds in our experiments was 0.633 mg (0.562–0.699 mg) (mean (95% confidence interval); $n=10$) and the seeds fell at an average speed of $U = 39.1 \text{ cm s}^{-1}$ (34.9–43.0 cm s⁻¹) (mean (95% confidence interval), $n=10$), leading to a mean $Re = 357$.

Flow field characterization of the SVR. To characterize the SVR, we performed direct numerical simulations of the flow past a permeable circular disk with aspect ratio $\chi = d/D = 0.0011$, Darcy number $Da = k/D^2 = 4.7 \times 10^{-6}$ and porosity $\varepsilon = 0.916$ at $Re = UD/\nu = 175$, in which k is the permeability of the disk, and U is the freestream speed (values for porosity and diameter were obtained from morphological analysis of samples—see Extended Data Table 2). We used a previously published modelling approach²⁵, in which we considered the steady, axisymmetric flow past the permeable disk. In the fluid domain, the steady-state Navier–Stokes equations are solved, and inside the permeable disk, the steady-state Darcy–Brinkmann equations are solved. Continuity of the velocity and pressure are enforced at the boundary between the fluid and porous domains, and the discretized system of equations is solved using COMSOL Multiphysics.

The results from our numerical modelling are shown in Extended Data Fig. 8. The flow around and through the porous disk is characterized by a marked slowdown of velocity u_z (Extended Data Fig. 8a). This is associated with a pressure increase upstream of the disk (Extended Data Fig. 8b). Across the disk, the flow velocity is conserved while the disk subtracts potential energy from the flow, resulting in a lower pressure downstream. Subsequently, the flow downstream of the disk is affected by the adverse pressure gradient between the high pressure in the far field and the low pressure in the region downstream of the disk. This pressure gradient further slows down the flow, which eventually reversed and led to the formation of a recirculation bubble due to viscous effects (Extended Data Fig. 8a, c). Further downstream, the gradual pressure recovery enables a lower pressure gradient, that is, a lower pressure force on the fluid, which therefore recovers its velocity by entrainment of momentum from the adjacent flow streams. This results in an asymptotic increase in velocity towards the far field. We quantified the numerical uncertainty (Y_{num}), which is the sum of the uncertainties due to the grid (Y_g) and the iterative convergence (Y_c) using the approach used in previous studies⁴⁵.

We found that the numerical uncertainty in the computed value of the streamwise length of the SVR was $Y_{\text{num}} < 0.02\%$ for the values of Re , Da and ε considered in this study.

The results from this numerical model provide insights into the pressure field and the general flow structure around the pappus. However, there are limitations to this simple model. The assumption of axisymmetry precludes any investigation of the observed symmetry breaking of the vortex (similar symmetry breaking is observed for impervious disks²³) or the breakdown of the SVR into vortex shedding at higher Re . In the latter case, to compute Re_c using this model, the assumption of time independence would also have to be relaxed.

Topology of the SVR. Topologically, the SVR is a degenerate focus with half-saddle separation (z_{su}) and reattachment (z_{sd}) points. For low Re , the vortex is axisymmetric; however, at some Re_c , the steady SVR loses its azimuthal symmetry by a regular bifurcation as illustrated in the schematic diagram in Extended Data Fig. 3e, f. The subsequent breakdown in stability of the SVR at $Re = Re_c$ is likely to occur through a Hopf bifurcation²⁴.

Design and microfabrication of replica pappi. Replica pappi of various porosities were designed using Wolfram Mathematica: first, a rectangle with length of $l \text{ mm}$ and varying widths of w was created using the rectangle function. The rectangle was then copied and rotated around a central point 20 times using the

Mathematica function GeometricTransformation to create a replica pappus with $n = 42$ filaments. The porosity of the disk depended on the width of the filament according to

$$\varepsilon = 1 - \frac{n w \{(l-b) + b/2\}}{\pi l^2}$$

in which $b = w/(2\tan(\pi/n))$. The resulting design was exported as a vector image for use in the microfabrication process. A length $l = 10$ mm (to explore the region $\text{Re} < 170$) and $l = 14$ mm (to explore $\text{Re} > 170$) was used.

The replica pappi were manufactured using photolithography and microfabrication techniques. A 1-μm thick layer of silicon oxide (SiO_2) was grown on a 3-inch silicon wafer substrate (thickness of 380 μm). After spincoating a 7-μm thick photoresistive film on the SiO_2 layer, the dandelion designs were patterned photolithographically onto the substrate. Afterwards, the exposed SiO_2 was removed by reaction ion etching in a plasma formed of CHF_3 and Ar. At this point, the dandelion structure was etched in deep reactive ion etching (Bosch process) using the photoresist and SiO_2 layer as an etch mask. Once the wafer was etched through completely, the dandelion structure was rinsed and bonded to an artificial stem to enable testing in the vertical wind tunnel.

Statistics. Throughout the paper, the 95% confidence intervals are obtained using bias-corrected and accelerated bootstrapping. All of the morphological data obtained from our dandelion samples was shown to be normally distributed, apart from the length filament (L).

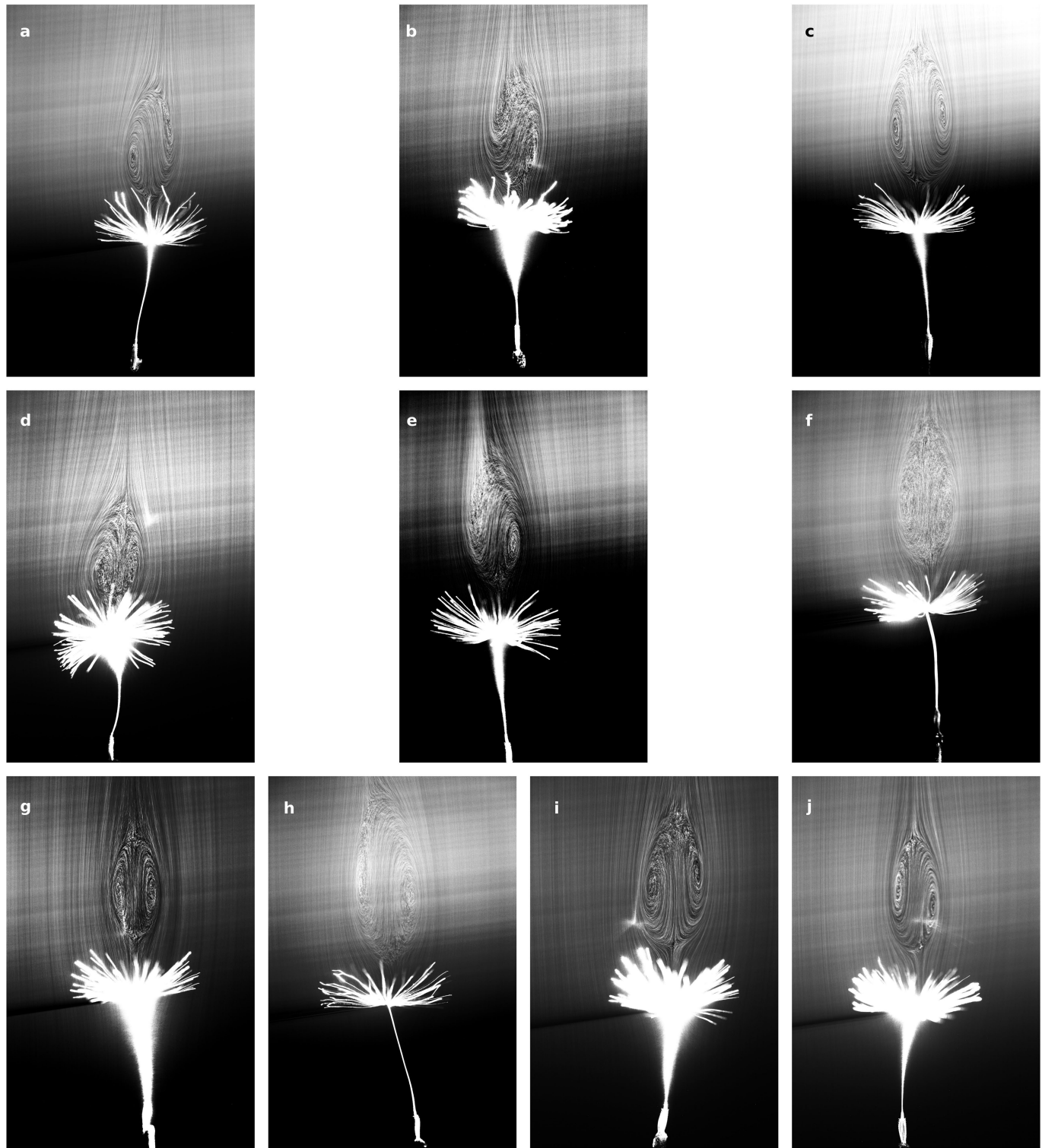
Reporting summary. Further information on research design is available in the Nature Research Reporting Summary linked to this paper.

Code availability. The codes used to produce Fig. 4a are available from Edinburgh DataShare^{35,36}.

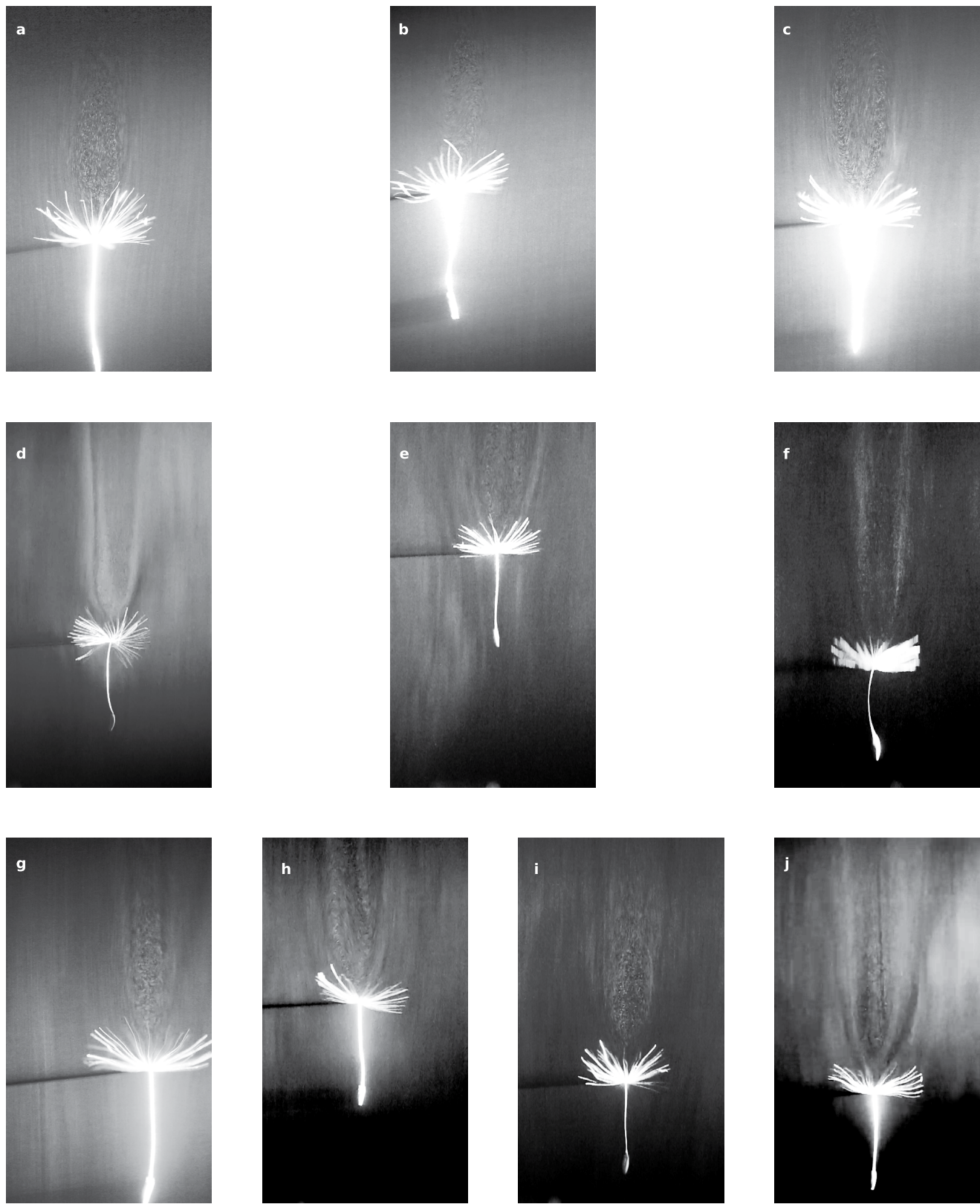
Data availability

The datasets generated and/or analysed during the current study are available from the corresponding author upon reasonable request.

35. Cummins, C., Nakayama, N., Viola, I. M. & Mastropaolo, E. MATLAB scripts for analysis of vortex shedding. <https://doi.org/10.7488/ds/2362> (2018).
36. Viola, I. M., Nakayama, N., Mastropaolo, E. & Cummins, C. Vortex shedding in the wake of a 75% porous disk. <https://doi.org/10.7488/ds/2363> (2018).
37. Dierick, M., Masschaele, B. & Hoorebeke, L. V. Octopus, a fast and user-friendly tomographic reconstruction package developed in LabView®. *Meas. Sci. Technol.* **15**, 1366–1370 (2004).
38. R Core Team. *R: A Language and Environment for Statistical Computing* <http://www.R-project.org/> (R Foundation for Statistical Computing, Vienna, Austria, 2013).
39. Sato, M., Bitter, I., Bender, M. A., Kaufman, A. E. & Nakajima, M. TEASAR: tree-structure extraction algorithm for accurate and robust skeletons. In *Proc. 8th Pacific Conference on Computer Graphics and Applications* (eds Barsky, B. A. et al.) 281–449 (IEEE, 2000).
40. Schneider, C. A., Rasband, W. S. & Eliceiri, K. W. NIH image to ImageJ: 25 years of image analysis. *Nat. Methods* **9**, 671–675 (2012).
41. Forster, B., Van De Ville, D., Berent, J., Sage, D. & Unser, M. Complex wavelets for extended depth-of-field: a new method for the fusion of multichannel microscopy images. *Microsc. Res. Tech.* **65**, 33–42 (2004).
42. Preibisch, S., Saalfeld, S. & Tomancak, P. Globally optimal stitching of tiled 3D microscopic image acquisitions. *Bioinformatics* **25**, 1463–1465 (2009).
43. White, C. M. The drag of cylinders in fluids at slow speeds. *Proc. R. Soc. A* **186**, 472–479 (1946).
44. Chwang, A. T. & Wu, T. Y.-T. Hydromechanics of low-Reynolds-number flow. Part 2. Singularity method for Stokes flows. *J. Fluid Mech.* **67**, 787–815 (1975).
45. Viola, I. M., Bot, P. & Riotte, M. On the uncertainty of CFD in sail aerodynamics. *Int. J. Numer. Methods Fluids* **72**, 1146–1164 (2013).

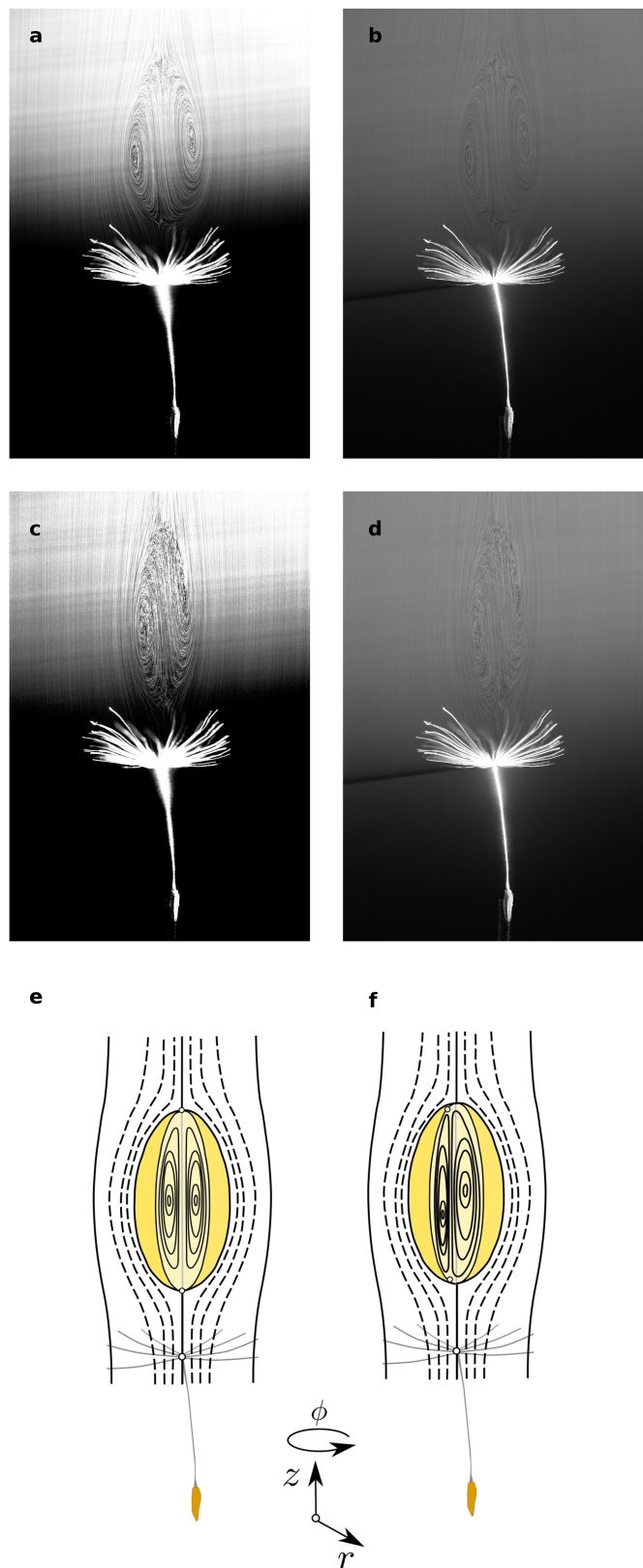


Extended Data Fig. 1 | SVR visualization of the wake of 10 fixed dandelion seeds. The flow speed is half of the terminal velocity of the seed. Each image was obtained using long-exposure photography.

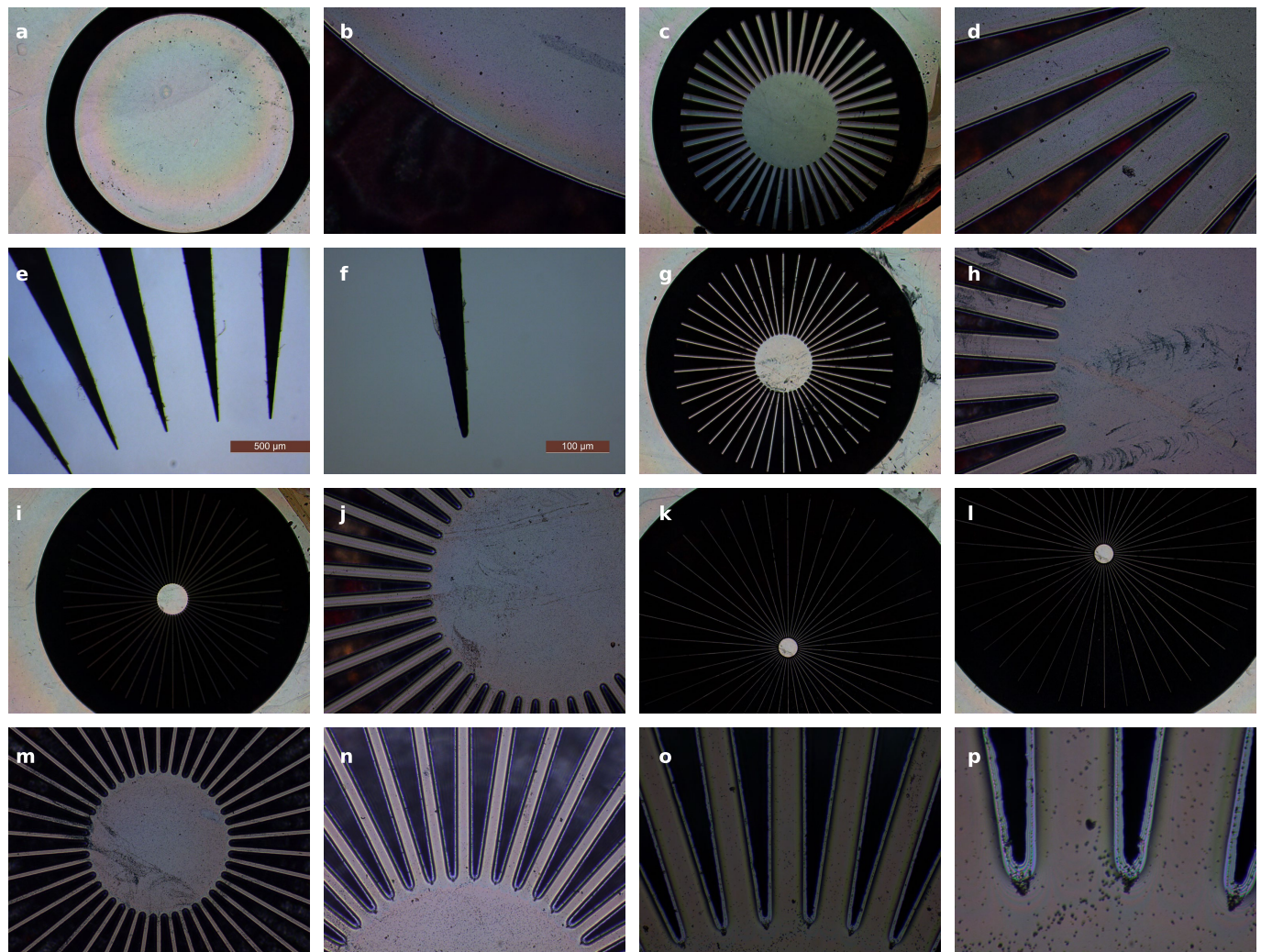


Extended Data Fig. 2 | SVR visualization of the wake of 10 freely flying dandelion seeds. **a–j,** Each image corresponds to a snapshot from a video of the flight of the dandelions in the wind tunnel. The images show the

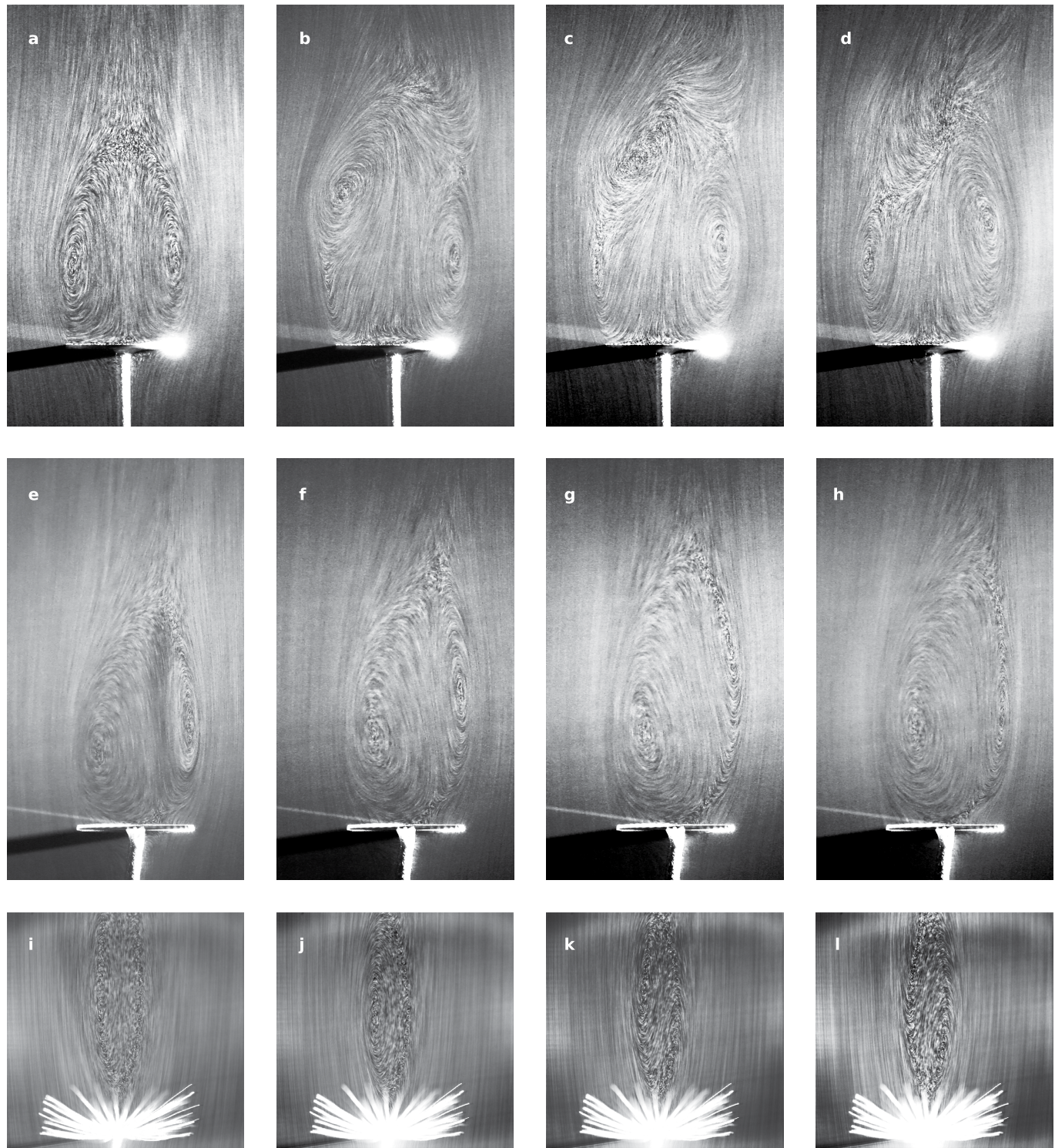
seeds as they pass through the laser sheet, and the SVR may be difficult to identify in some panels because of the orientation of the laser sheet with respect to the axis of the SVR.



Extended Data Fig. 3 | The breakdown in symmetry in the SVR of dandelion seeds. **a, b**, At low speeds, the SVR is axisymmetric. **a**, Contrast-enhanced image. **b**, Original image. **c, d**, At higher speeds, this symmetry is lost. **c**, Contrast-enhanced image. **d**, Original image. **a–d**, Experiments were repeated independently on $n = 10$ biological samples, with similar results. **e, f**, The axisymmetry of SVR at low Re (**e**) breaks down at higher Re (**f**).

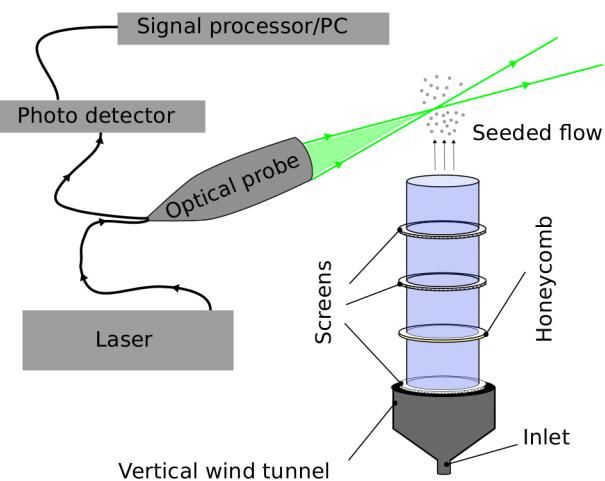
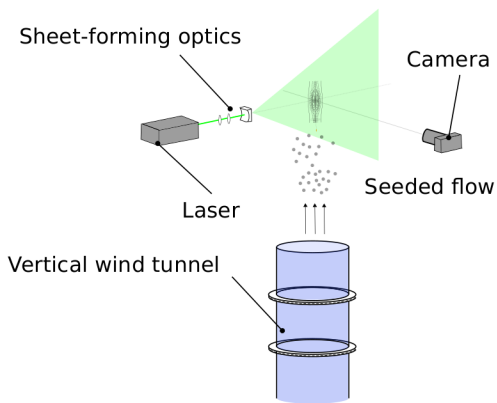
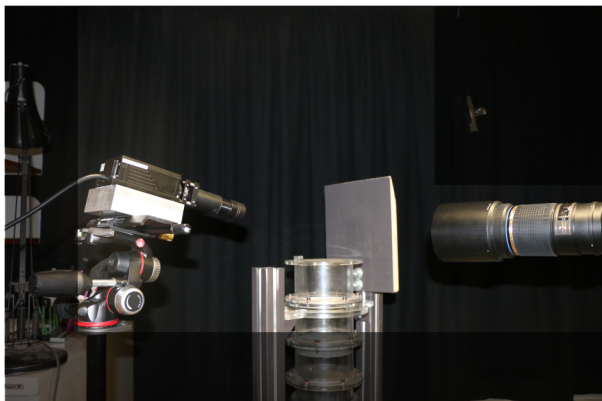


Extended Data Fig. 4 | Images of porous disks showing the resolution of the technique for disks of various porosities. **a, b,** Impervious disk. **c–f,** A disk with 33% porosity. **g, h,** A disk with 55% porosity. **i, j,** A disk with 75% porosity. **k–p,** A disk with 89% porosity.

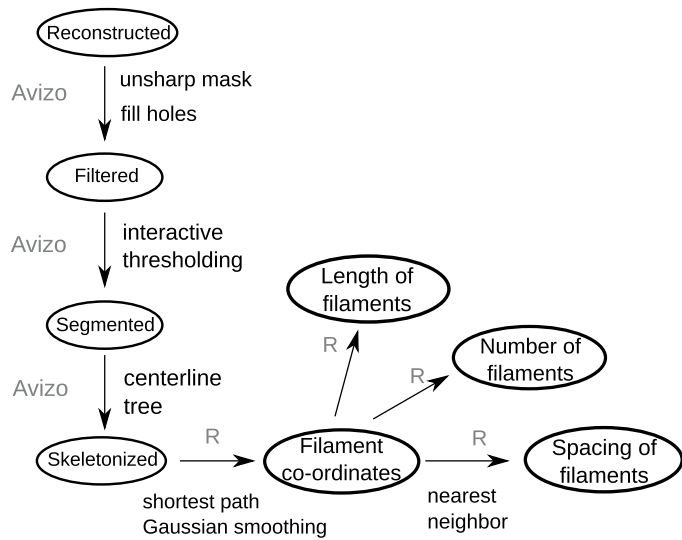


Extended Data Fig. 5 | Steady and unsteady wake behind porous disks and pappi. Video snapshots are shown. **a–d**, The flow visualization behind a solid disk, with a steady wake (**a**) and an unsteady wake at three time points within one period of vortex shedding (**b–d**). **e–h**, The flow around

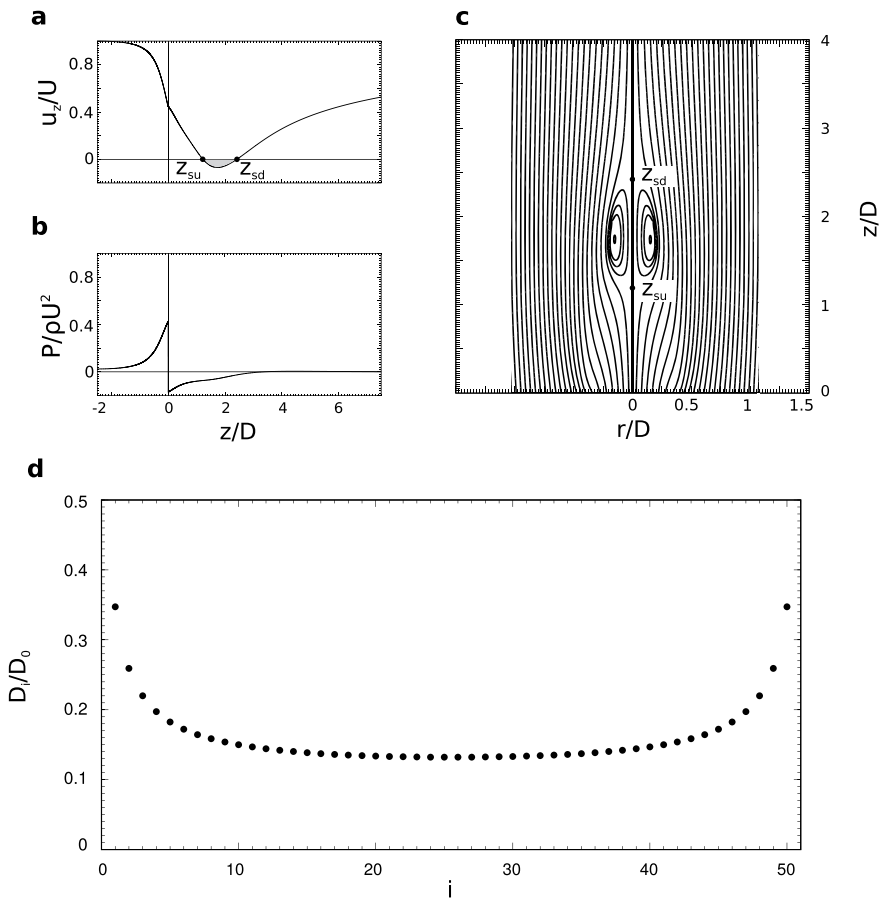
a porous disk ($\varepsilon = 0.75$) with a steady wake (**e**) and an unsteady wake at three time points within one period of vortex shedding (**f–h**). **i–l**, The wake behind a dandelion sample with a steady SVR (**i**) and at three time points within one period of vortex shedding (**j–l**).

a**b****c**

Extended Data Fig. 6 | The experimental setup for laser Doppler anemometry and flow visualization. **a, b,** Schematic drawings of the experimental setup for laser Doppler anemometry to measure the flow speed and turbulent intensity in the wind tunnel (**a**) and the experimental setup for flow visualization in the wind tunnel using a CW laser and high-speed camera (**b**). **c,** Photograph of the actual experimental setup for flow visualization.



Extended Data Fig. 7 | Workflow for post-processing of the μCT scan data. Image processing workflow for analysis of μCT data indicating the algorithms performed and the software used (Avizo or R).



Extended Data Fig. 8 | The flow past a porous disk using direct numerical simulations and boundary integral methods. **a–c**, The axial velocity u_z/U (**a**), pressure $p/\rho U^2$ (**b**) and streamlines (**c**), showing the presence of an SVR with upstream and downstream stagnation points z_{su}

and z_{sd} , respectively. **d**, The reduction in the drag force on filaments within an array moving at slow speeds calculated using a boundary integral method. The force D_i on the i th filament of a rectangular pappus, divided by the drag force for an isolated filament D_0 .

Extended Data Table 1 | μ CT scan-acquisition settings

X-ray energy	25 keV
X-ray power	14 W
Distance (X-ray to sample)	71 mm
Acquisition mode	reflectance
Camera type	Perkin-Elmer
Distance (camera to X-ray)	549.5 mm
Filter	none
Pixel size	0.2 mm
No. projections	2000
Exposure	2s

Extended Data Table 2 | Morphological data of dandelion seeds

	Diameter d (μm)	Length L (mm)	Filaments n	Porosity ϵ
mean =	16.3	7.41	100	0.916
CI =	15.7–17.0	7.35–7.46	95–106	0.907–0.923
n =	10	937	10	10

Data are shown as mean and 95% confidence intervals and the number of samples is shown.

Reporting Summary

Nature Research wishes to improve the reproducibility of the work that we publish. This form provides structure for consistency and transparency in reporting. For further information on Nature Research policies, see [Authors & Referees](#) and the [Editorial Policy Checklist](#).

Statistical parameters

When statistical analyses are reported, confirm that the following items are present in the relevant location (e.g. figure legend, table legend, main text, or Methods section).

n/a Confirmed

- The exact sample size (n) for each experimental group/condition, given as a discrete number and unit of measurement
- An indication of whether measurements were taken from distinct samples or whether the same sample was measured repeatedly
- The statistical test(s) used AND whether they are one- or two-sided
Only common tests should be described solely by name; describe more complex techniques in the Methods section.
- A description of all covariates tested
- A description of any assumptions or corrections, such as tests of normality and adjustment for multiple comparisons
- A full description of the statistics including central tendency (e.g. means) or other basic estimates (e.g. regression coefficient) AND variation (e.g. standard deviation) or associated estimates of uncertainty (e.g. confidence intervals)
- For null hypothesis testing, the test statistic (e.g. F , t , r) with confidence intervals, effect sizes, degrees of freedom and P value noted
Give P values as exact values whenever suitable.
- For Bayesian analysis, information on the choice of priors and Markov chain Monte Carlo settings
- For hierarchical and complex designs, identification of the appropriate level for tests and full reporting of outcomes
- Estimates of effect sizes (e.g. Cohen's d , Pearson's r), indicating how they were calculated
- Clearly defined error bars
State explicitly what error bars represent (e.g. SD, SE, CI)

Our web collection on [statistics for biologists](#) may be useful.

Software and code

Policy information about [availability of computer code](#)

Data collection

Picoscope 6

Comsol Multiphysics 5.3a

MATLAB R2016a

MATLAB packages:

PIVLab 1.41

Wolfram Mathematica 10.2

Avizo, version 9.0.1 (FEI, ThermoFisher Scientific)

R, version 3.3.0

R packages:

igraph v1.1.2

smoother v1.1

spatstat v1.54-0

ImageJ, version 1.51w

ImageJ plugins:
Extended Depth of Field

Data analysis

Picoscope 6
Comsol Multiphysics 5.3a
MATLAB R2016a
MATLAB packages:
PIVLab 1.41
Wolfram Mathematica 10.2
Avizo, version 9.0.1 (FEI, ThermoFisher Scientific)
R, version 3.3.0
R packages:
igraph v1.1.2
smoother v1.1
spatstat v1.54-0
ImageJ, version 1.51w
ImageJ plugins:
Extended Depth of Field

For manuscripts utilizing custom algorithms or software that are central to the research but not yet described in published literature, software must be made available to editors/reviewers upon request. We strongly encourage code deposition in a community repository (e.g. GitHub). See the Nature Research [guidelines for submitting code & software](#) for further information.

Data

Policy information about [availability of data](#)

All manuscripts must include a [data availability statement](#). This statement should provide the following information, where applicable:

- Accession codes, unique identifiers, or web links for publicly available datasets
- A list of figures that have associated raw data
- A description of any restrictions on data availability

The datasets generated during and/or analysed during the current study are available from the corresponding author upon reasonable request.

Field-specific reporting

Please select the best fit for your research. If you are not sure, read the appropriate sections before making your selection.

Life sciences Behavioural & social sciences Ecological, evolutionary & environmental sciences

For a reference copy of the document with all sections, see nature.com/authors/policies/ReportingSummary-flat.pdf

Life sciences study design

All studies must disclose on these points even when the disclosure is negative.

Sample size Ten samples was deemed sufficient for the purposes of these experiments.

Data exclusions Seeds for flow visualization were selected that were intact and not damaged in transport/storage.

Replication All images are representative of 10 independent repeats. For all dandelion experiments, 10 samples were used. For each of the porous disk experiments, a single porous disk was used due to the challenging nature of making the disks.

Fig. 1: We observed similar results to a-c and e-f in n=10 independent biological replicates. In g and h, similar results were obtained in 10 similar experiments for (g) and 18 similar experiments for (h).

Fig. 2: The 95% confidence intervals for the mean values were obtained using bias-corrected accelerated bootstrapping. The number of technical repeats performed for each data point is indicated in the final two columns of Re-Cd-Natural-Seeds.csv in the source data.

Fig. 3: (d) Similar results were obtained in 18 independent experiments (each experiment at a different Reynolds number). The images in e and f were obtained for a single disk.

Fig. 4: (a) The error bars in the vertical direction on the green data point is the 95% confidence interval in the critical Reynolds number, obtained by bias-corrected bootstrapping the data from 10 dandelion seeds. The error bars in the horizontal direction on the green data point indicate the 95% confidence interval in the porosity of the papilla, obtained by bias-corrected bootstrapping the data from the 10 dandelion seeds. Each black dot in (a) is obtained by performing experiments of varying speed on a single disk at the stated porosity. (b) The vertical

errorbars give the 95% confidence interval for the mean Reynolds number of freely flying seeds, obtained through bias-corrected accelerated bootstrapping, and are identical to the horizontal red error bars in Fig 2a. The horizontal errorbars in (b) indicate the error due to the finite resolution of the microscope, which was obtained by computing the porosity of a sample at 5 different resolutions and measuring the error found at the resolution used to obtain the mean values that are used in the paper.

Extended Data Fig. 5: (a) Independent experiments were performed 5 times with similar results (each experiment at a different Reynolds number). (b-d) Independent experiments were repeated 10 times with similar results (each experiment at a different Reynolds number). (e) Independent experiments were repeated 7 times with similar results (each experiment at a different Reynolds number). (f-h) Independent experiments were repeated 10 times with similar results (each experiment at a different Reynolds number). (i-l) The experiments were repeated independently for n=10 biological replicates with similar results.

Randomization Ten plants were grown, and a seed was chosen from a randomly selected seed head per plant.

Blinding Sample selection was not blind to ensure samples selected were not damaged.

Reporting for specific materials, systems and methods

Materials & experimental systems

n/a	Involved in the study
<input checked="" type="checkbox"/>	Unique biological materials
<input checked="" type="checkbox"/>	Antibodies
<input checked="" type="checkbox"/>	Eukaryotic cell lines
<input checked="" type="checkbox"/>	Palaeontology
<input type="checkbox"/>	Animals and other organisms
<input checked="" type="checkbox"/>	Human research participants

Methods

n/a	Involved in the study
<input checked="" type="checkbox"/>	ChIP-seq
<input checked="" type="checkbox"/>	Flow cytometry
<input checked="" type="checkbox"/>	MRI-based neuroimaging

Animals and other organisms

Policy information about [studies involving animals; ARRIVE guidelines](#) recommended for reporting animal research

Laboratory animals

Laboratory animals were not involved in the experiments.

Wild animals

Wild animals were not involved in the experiments.

Field-collected samples

Dandelion seeds were collected from a single plant growing in Edinburgh (55.922684, -3.170703) in April 2014. Seeds were germinated in 10 cm round Petri dishes containing distilled water in 16h light/8h dark conditions (100 µmol m⁻² s⁻¹ 25°C day, 23°C night) for 2 weeks. They were then transplanted to 7 × 7 × 8 cm pots with soil/perlite mix (60% v/v Levington's F2+S (Everris), 24% v/v standard perlite (Sinclair), 16% v/v washed horticultural sand, 0.3 g/L Exemptor (Everris)) and grown in 16h light/8h dark conditions in a controlled environment room (100 µmol m⁻² s⁻¹, 21°C) for 4 weeks. Plants were transplanted into 4 L pots with peat/sand mix (83% v/v medium peat (Clover), 21% v/v washed horticultural sand, 3 g/L garden limestone (Arthur Bowers), 1 g/L Osmocote Exact Standard 5-6 months (Everris), 0.4 g/L Exemptor (Everris)) and transferred to a glasshouse with ambient light supplemented to ensure a 16h day (minimum intensity of 250 µmol m⁻² s⁻¹, 06:00 – 22:00 GMT) and temperature of 21°C day, 18°C night. For µCT scans, seeds used were the offspring of the original collected plants. For all other experiments, seeds were from the following generation. All of these seeds from the second generation originated from the same parent plant. As *T. officinale* is apomictic, all seeds are assumed to be genetically identical. Throughout the paper, we use the term dandelion "seed" as a shorthand to refer to the entire diaspore (fruit-pappus unit).